Journal of Materials Chemistry A

ROYAL SOCIETY OF CHEMISTRY

PAPER

View Article Online
View Journal | View Issue

Cite this: J. Mater. Chem. A, 2022, 10, 5981

A MnO_x enhanced atomically dispersed iron–nitrogen–carbon catalyst for the oxygen reduction reaction†

Shichao Ding, ‡[a] Zhaoyuan Lyu,‡[a] Erik Sarnello,[b] Mingjie Xu,[c] Lingzhe Fang,[b] Hangyu Tian,[a] Sam Ellery Karcher,[a] Tao Li,[bd] Xiaoqing Pan,[c] John McCloy,[a] Guodong Ding,[e] Qiang Zhang,[e] Qiurong Shi,[a] Dan Du,[a] Jin-Cheng Li,*[a] Xiao Zhang*[f] and Yuehe Lin*[aef]

Cost-effective and highly efficient Fe–N–C single-atom catalysts (SACs) have been considered to be one of the most promising potential Pt substitutes for the cathodic oxygen reduction reaction (ORR) in proton exchange membrane fuel cells (PEMFCs). Nevertheless, they are subject to severe oxidative corrosion originating from the Fenton reaction, leading to poor long-time durability of PEMFCs. Herein, we propose a MnO_x engineered Fe–N–C SAC (Mn–Fe–N–C SAC) to reduce and even eliminate the stability issue, as MnO_x accelerates the degradation of the H_2O_2 by-product *via* a disproportionation reaction to weaken the Fenton reaction. As a result, the Mn–Fe–N–C SAC shows an ultralow H_2O_2 yield and a negligible half-wave potential shift after 10 000 continuous potential cycles, demonstrating excellent ORR stability. Besides, the Mn–Fe–N–C SAC also shows an improved ORR activity compared to the common Fe–N–C SAC. Results show that the MnO_x interacts with the Fe–N_x site, possibly forming Fe–Mn or Fe–O–Mn bonds, and enhances the intrinsic activity of single iron sites. This work provides a method to overcome the stability problem of Fe–N–C SACs while still yielding excellent catalytic activity, thus showing great promise for application in PEMFCs.

Received 24th August 2021
Accepted 5th November 2021

DOI: 10.1039/d1ta07219f

rsc.li/materials-a

Introduction

As one of the most promising next-generation power sources for automobiles, proton exchange membrane fuel cells (PEMFCs) have received enormous attention.[1,2] Nevertheless, the sluggish oxygen reduction reaction (ORR) at the cathode hinders the output performance of PEMFCs.[3] To achieve acceptable performance, highly efficient ORR catalysts are greatly needed. Nowadays, it is believed that the desirable ORR catalysts are Pt and its alloys, such as commercial Pt nanoparticles loaded on carbon black (Pt/C). Nevertheless, they are subject to prohibitive prices and inadequate durability, thereby limiting their widespread application.[4–6] Therefore, there is an ongoing search for inexpensive non-Pt catalysts that can rival the performance of Pt.[7]

Extensive research has been performed on non-precious metal catalysts (NPMCs) to overcome the aforementioned challenges, especially for synthesizing high-efficiency and low-cost Fe–N–C single-atom catalysts (SACs).[8–14] Many methods have been used to design Fe–N–C SACs to improve the ORR activity under acidic conditions, and some of them are nearly as effective as Pt/C.[15] For instance, Wang *et al.* developed an Fe–N–C catalyst that exhibited good ORR performance in acidic solution with high half-wave potential ($E_{1/2}$), decreasing the activity gap between current NMPCs and Pt/C catalysts.[16] In our previous work we designed single-iron atoms on porous nitrogen-doped carbon nanowires which also exhibited an impressive $E_{1/2}$ of 0.82 V as well as outstanding kinetic current density.[17] Unfortunately, the Fe–N–C SACs' stability is still not satisfactory, which limits their further vital applications.

One of the most important reasons is that the H_2O_2 side-product is produced *via* a two-electron pathway, accelerating the formation of dissolved Fe ions from active sites. Even worse, the dissolved Fe ions can combine with H_2O_2, participating in the Fenton reaction, which will generate a highly powerful oxidizing agent, radical oxygen species (ROS).[18] As a result, the

[a]School of Mechanical and Materials Engineering, Washington State University, Pullman, WA, 99164, USA. E-mail: yuehe.lin@wsu.edu; jin-cheng.li@wsu.edu
[b]Department of Chemistry and Biochemistry, Northern Illinois University, DeKalb, IL, 60115, USA
[c]Irvine Materials Research Institute (IMRI), Department of Materials Science and Engineering, University of California, Irvine, CA, 92697, USA
[d]X-ray Science Division, Argonne National Laboratory, Lemont, IL, 60439, USA
[e]Department of Chemistry, Washington State University, Pullman, Washington 99164, USA
[f]School of Chemical Engineering and Bioengineering, Washington State University, USA. E-mail: x.zhang@wsu.edu

† Electronic supplementary information (ESI) available. See DOI: 10.1039/d1ta07219f

‡ Shichao Ding and Zhaoyuan Lyu have contributed equally to this work.

ROS and H_2O_2 continue to attack the active sites of catalysts, which leads to the low stability of Fe–N–C SACs and damages the membrane electrode assembly (MEA), thereby accelerating performance degradation.[19]

Recently, carbon-supported Mn-based NPMCs have been proposed to boost the ORR due to their considerable catalytic activity and good stability.[20,21] For example, Yu *et al.* developed MnO_2 nanofilms grown on hollow graphene spheres, which significantly improved the ORR catalytic activity compared with that of regular hollow graphene spheres.[22] Introducing Mn into a N–C-based catalyst can enhance the charge transfer and regulate the abundant defects, thereby yielding a better ORR catalytic performance.[23] Most importantly, the Fenton reaction between Mn ions and H_2O_2 is very weak, and Mn-based NPMCs such as MnO_x can degrade H_2O_2 by virtue of a disproportionation reaction. These features of Mn species can inhibit the Fenton reaction effectively,[24] and these advantages motivate us to use MnO_x to enhance the stability of Fe–N–C catalysts.

In this work, we adopt a simple but efficient strategy to design a MnO_x engineered Fe–N–C single-atom catalyst (Mn–Fe–N–C SAC) by using MnO_x-coated iron-doped polypyrrole nanotubes (Fe–PPy NTs) as the precursor. The introduced MnO_x can be used as a co-catalyst to improve the catalytic ability and stability. The atomically dispersed iron active sites in the Mn–Fe–N–C SAC were shown by aberration-corrected scanning transmission electron microscopy (AC STEM) and extended X-ray absorption fine structure (EXAFS). Besides, the MnO_x interacts with Fe–N_x sites, possibly forming Fe–Mn or Fe–O–Mn bonds. Such feature could endow the Mn–Fe–N–C SAC with a better ORR performance than that of the common Fe–N–C SAC under acidic conditions. Most importantly, MnO_x could reduce the Fenton reaction and enhance the long-term durability of the SAC significantly. This facile MnO_x engineering process demonstrates a new method for the preparation of Fe–N–C-based SACs for fuel cells with sufficient ORR activity and excellent stability.

The schematic illustration of the synthesis of the Mn–Fe–N–C SAC is shown in Fig. 1a. Methyl orange (MO) was dissolved in distilled water, and then iron(III) chloride ($FeCl_3$) was added to form an oxidized MO template. A polymerization step was conducted to achieve Fe–PPy NTs after adding pyrrole. Scanning electron microscopy (SEM) and transmission electron microscopy (TEM) results demonstrate that the obtained Fe–PPy NTs have a uniform tubular morphology with a diameter of ~200 nm (Fig. S1† and 1b). The Fe-doped PPy NTs were dispersed in a $KMnO_4$ solution for MnO_x-coating (Fig. 1c). Subsequently, the Mn–Fe–N–C SAC was obtained from a pyrolytic process and a second NH_3 heat treatment. An Fe–N–C SAC without the MnO_x coating was also synthesized for comparison. The nanotubular structure was well maintained after pyrolysis (Fig. 1d and S2†), and a few MnO_x crystals can still be found in the Mn–Fe–N–C SAC, which are marked in red circles (Fig. 1d).

Bright field STEM (BF-STEM) imaging was further utilized to investigate the microstructures of the Mn–Fe–N–C SAC and Fe–N–C SAC. As shown in Fig. 2a and b, both SACs exhibit a distorted graphitic carbon structure. This structure usually accompanies plentiful defects and edges, which provide ample room for hosting a large number of isolated iron atoms.[25] These enriched defects and edges are quantitatively evaluated using the ratio of C-sp^2 detected by X-ray photoelectron spectroscopy (XPS).[26,27] Compared to the common Fe–N–C SAC, the Mn–Fe–N–C SAC shows a lower ratio of C-sp^2, indicating that the Mn–Fe–N–C SAC has a lower degree of graphitization as well as more abundant defects and edges (Fig. S3†).

Raman characterization was further utilized to track their graphitization degree. As shown in Fig. 2c, the two peaks at

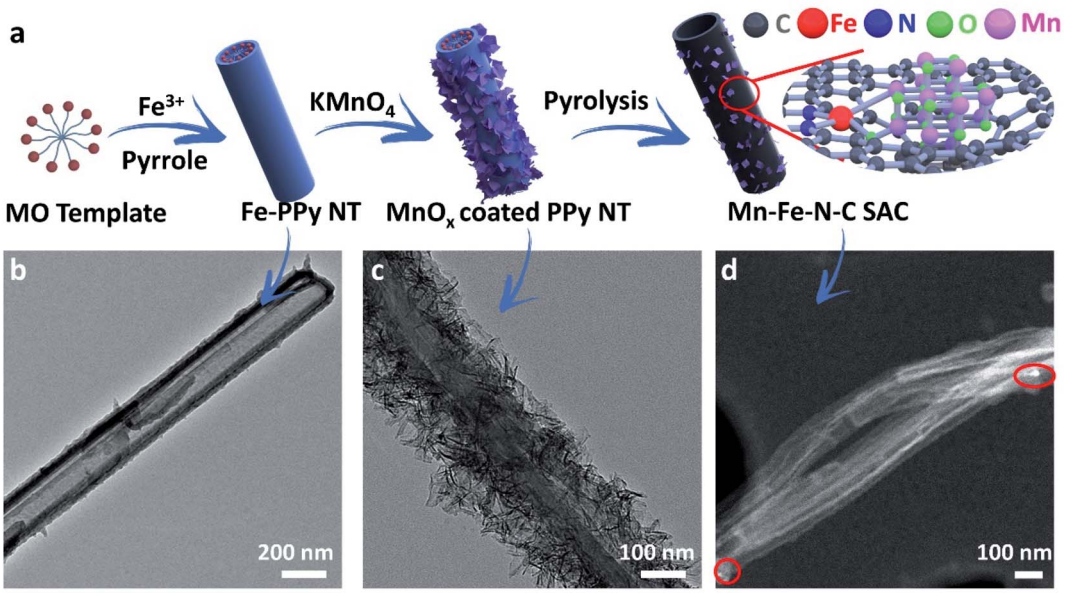

Fig. 1 (a) Schematic illustration of the synthesis of the Mn–Fe–N–C SAC; TEM images of (b) an Fe–PPy nanotube, (c) a MnO_x-coated Fe–PPy nanotube, and (d) the Mn–Fe–N–C SAC.

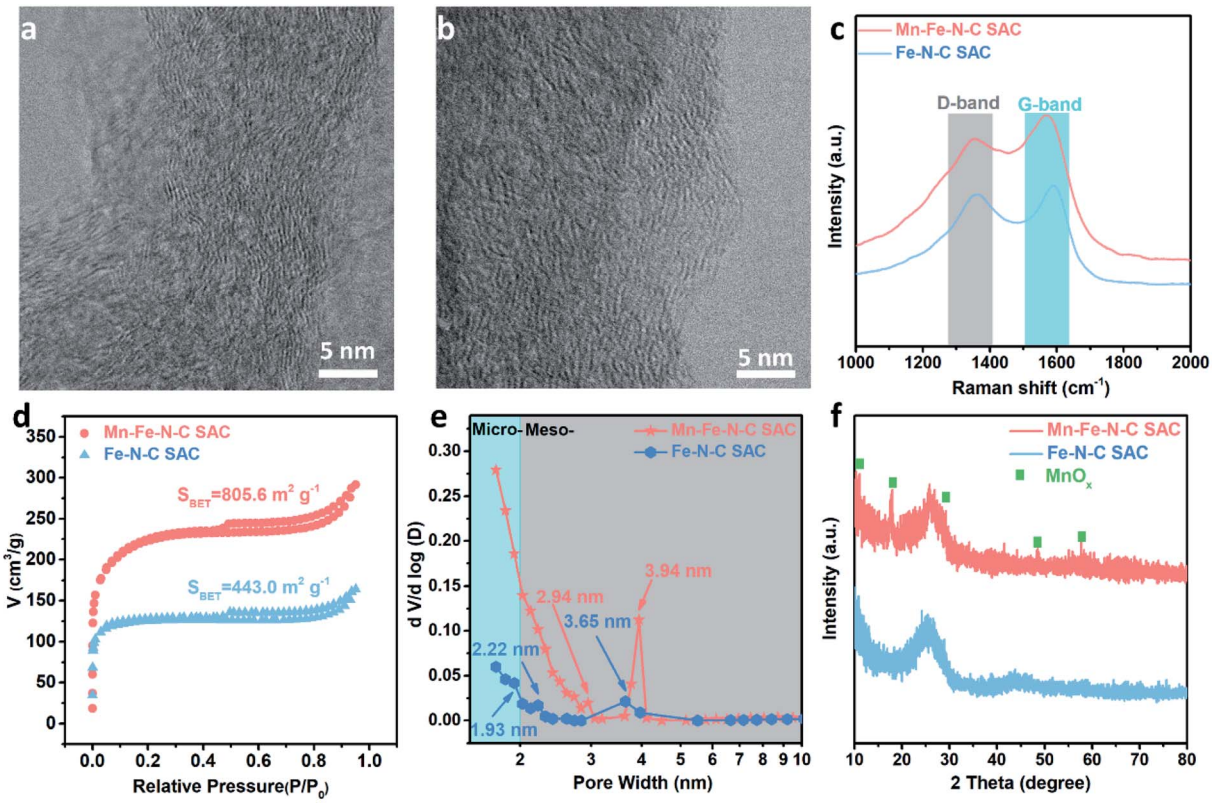

Fig. 2 BF-STEM images of (a) Mn–Fe–N–C SAC and (b) Fe–N–C SAC. (c) Raman spectra, (d) N_2 adsorption–desorption isotherm curves, (e) pore size distribution curves and (f) XRD patterns of the Mn–Fe–N–C SAC and Fe–N–C SAC.

around 1356 cm^{-1} and 1583 cm^{-1} can be identified as the D band and G band, respectively.[28] The quantity of defects and structural imperfections in carbon materials is reflected by the intensity ratio of the two bands (I_D/I_G).[29] Herein, the I_D/I_G of the Mn–Fe–N–C SAC (~0.92) is larger than that of the Fe–N–C SAC (~0.90), which illustrates that more defects are produced by MnO_x engineering, in good agreement with the XPS results (Fig. S3†).[30]

Nitrogen adsorption–desorption tests were further conducted to investigate the details of the specific surface area and pore structure in the Mn–Fe–N–C SAC. In Fig. 2d, we can see a strong adsorption at a relatively low pressure zone of $P/P_0 < 0.01$ and a type IV isotherm curve hysteresis (H4), which is a consequence of existing micropores and mesopores. The H4 hysteresis loop represents narrow, slit-like pores and particles with irregular-shaped pores, which is well in line with the morphology of the materials.[31] The pore size distributions (Fig. 2e) show that the pore sizes of both samples are below 4.0 nm. Nevertheless, compared to the Fe–N–C SAC, a MnO_x-coating process endows the Mn–Fe–N–C SAC with greater pore volume and higher Brunauer–Emmett–Teller (BET) surface area, which can contribute to faster mass transport. There are two etching effects on the precursor and final obtained material which are attributed to the higher BET specific surface area of the Mn–Fe–N–C SAC. One is the etching effect of $KMnO_4$ on the PPy nanotube precursor, resulting in the precursor having more defects and therefore more abundant pore structures.[27] The other is the etching effect of MnO_x. High temperature results in MnO_x evaporation, during which carbon species around MnO_x would be taken away in the form of gas species. X-ray diffraction (XRD) was performed to evaluate the crystallinity (Fig. 2f). No XRD patterns from iron species are observed, but several apparent peaks corresponding MnO_x are observed in the Mn–Fe–N–C SAC,[32] suggesting that some MnO_x remained in the catalyst after pyrolysis, in agreement with the TEM results.

XPS was further utilized to probe the surface chemical composition and chemical states. Fig. S4† shows the elements present and their contents in both SACs. The Fe content in the Mn–Fe–N–C SAC is 0.22 at%, almost the same as that of the Fe–N–C SAC (0.23 at%). The Mn content in the Mn–Fe–N–C SAC is 0.52 at%, while no Mn signal is detected in the Fe–N–C SAC sample (Fig. S4 and S5†). As shown in Fig. 3a, the Mn $2p_{3/2}$ spectrum of the Mn–Fe–N–C SAC can be split into three bands with energy peaks at 639.5, 641.1, and 643.2 eV, which are ascribed to Mn^{2+}, Mn^{3+}, and Mn^{4+} species based on bonding energies,[33,34] respectively, revealing the co-existence of three kinds of Mn species on the surface of the Mn–Fe–N–C SAC. The ratio of $(Mn^{2+} + Mn^{3+})/Mn_{total}$ based on the XPS peak areas is 0.53, implying that abundant oxygen vacancies exist in MnO_x.[35] The N 1s spectra can be fitted into pyridinic N, pyrrolic N, graphitic N, and oxidized N (Fig. S6†). Defective N species (pyridinic and pyrrolic N) are acknowledged as coordination sites for single Fe atoms (Fe–N_x).[36] Compared to the Fe–N–C SAC (Fig. 3b), the Mn–Fe–N–C SAC has a higher content of

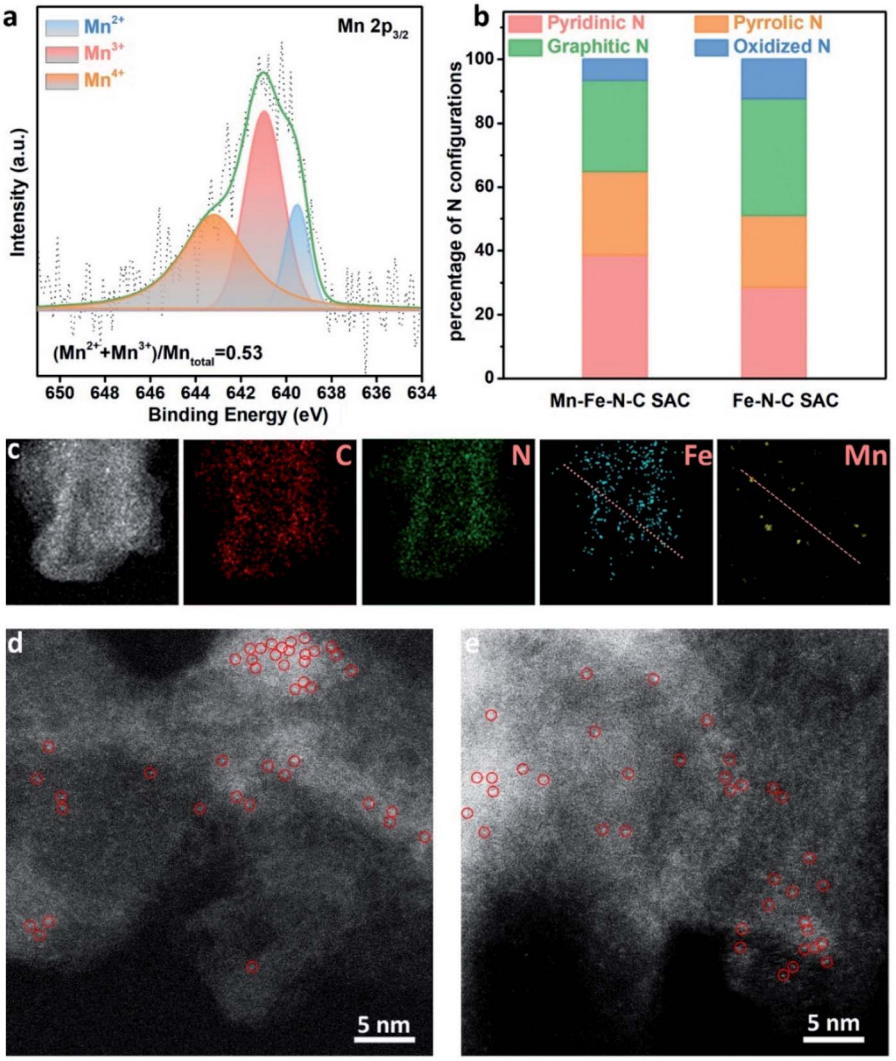

Fig. 3 (a) Mn $2p_{3/2}$ spectra of the Mn–Fe–N–C SAC. (b) The percentage of N configurations in the Mn–Fe–N–C SAC and Fe–N–C SAC by XPS measurements. (c) HAADF-STEM image and elemental maps of the Mn–Fe–N–C SAC; the linear scan profiles in Fig. S7† are derived from the red lines in the Fe and Mn maps of (c). HAADF-STEM images of (d) Mn–Fe–N–C SAC and (e) Fe–N–C SAC (isolated atom sites are marked with red circles as examples).

defective N species, suggesting that it has more defects (or micropores) to host isolated Fe–N_x coordination sites.[37–39]

Moreover, a component comparison, especially of the Fe and Mn contents of the two SACs, was conducted by TEM imaging along with energy-dispersive X-ray spectroscopy (EDS). As shown in Fig. 3c, Fe elements are uniformly distributed in the Mn–Fe–N–C SAC. Some MnO_x nanocrystals are also found, which is well in line with the above TEM and XRD results. Furthermore, there are spatial overlaps between Mn and Fe in the EDS linear scan, indicating the possible existence of chemical bonds between Fe and Mn (Fig. S7†). Furthermore, high-angle annular dark-field STEM (HAADF-STEM) images reveal that individual Fe atoms, marked by red circles, are homogeneously dispersed throughout the Mn–Fe–N–C SAC (Fig. 3d) and Fe–N–C SAC (Fig. 3e).

We performed X-ray absorption spectroscopy analysis to unravel the local environment of Fe atoms further. According to the Fe K-edge X-ray absorption near edge structure (XANES) spectra (Fig. 4a), the Fe absorption edge positions in both the Mn–Fe–N–C SAC and Fe–N–C SAC are between those of the Fe(II) and Fe(III) states, which is in good agreement with XPS results (Fig. S8†) and previous reports.[40,41] The k^3-weighted Fourier-transformed (FT) extended X-ray absorption fine structure (EXAFS) spectra (Fig. 4b) show that both SACs exhibit a prominent peak at around 1.42 Å, which is consistent with the Fe–N_4 peak from FePc, suggesting the presence of atomically dispersed Fe–N_x sites. Moreover, different from that of the Fe–N–C SAC, the curve of the Mn–Fe–N–C SAC also shows two peaks at around 1.75 Å and 2.39 Å, which may be attributed to Fe–O and Fe–Mn backscattering peaks, respectively.[42,43] This means that MnO_x still exists in the SACs after heat-treatment/acid washing and may form Fe–O–Mn or Fe–Mn bonds. The fitting results in Fig. 4c and S9† reveal the Fe–N scattering path and the existence of Fe–O–Mn and Fe–Mn coordination (Table

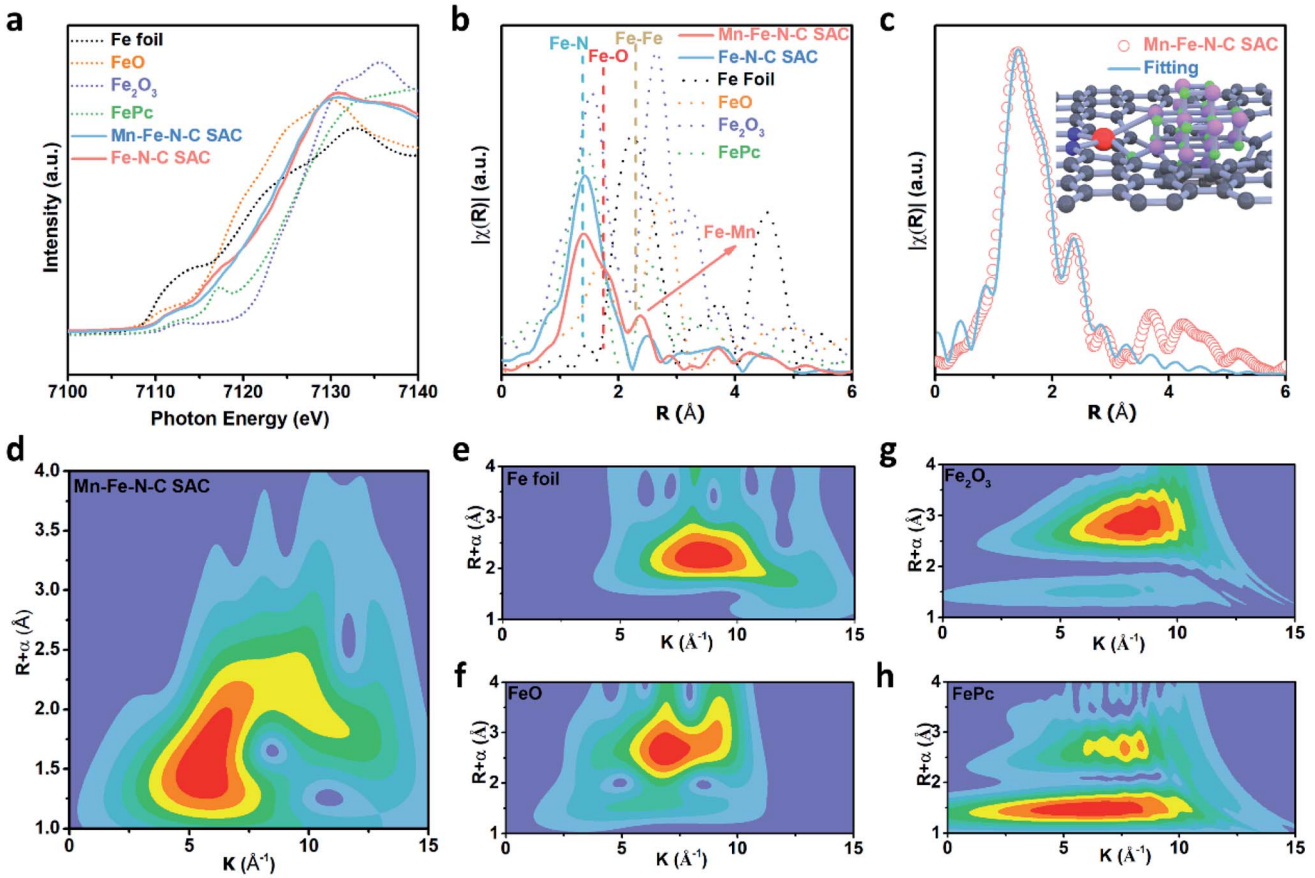

Fig. 4 (a) Fe K-edge XANES spectrum of the two SACs and reference samples of FePc, Fe foil, FeO and Fe_2O_3. (b) FT k^3-weighted EXAFS spectrum of Mn–Fe–N–C SAC, Fe–N–C SAC, FePc, FeO, Fe_2O_3, and Fe foil. (c) FT-EXAFS fitting curves of Mn–Fe–N–C SAC. The blue, gray, and red, purple, and green balls represent the N, C, Fe, Mn, and O atoms, respectively. Wavelet transform (WT) of (d) Mn–Fe–N–C SAC, (e) Fe foil, (f) FeO, (g) Fe_2O_3, and (h) FePc.

S1†). The coordination structure of the Fe active site can be coordinated by planar O, Mn, and two N atoms (inset of Fig. 4c). Wavelet transform (WT) can show remarkable resolution in k and R spaces simultaneously and analyze Fe K-edge EXAFS oscillations here. In Fig. 4d, the intensity maxima at ~5 $Å^{-1}$ for the Mn–Fe–N–C SAC can be attributed to the Fe–N bonding. No intensity maximum corresponding to Fe–Fe is observed when compared with the WT contour plots of references including Fe foil, FeO, and Fe_2O_3 (Fig. 4f–h).[44] Therefore, by combining all the above structures, chemical states, and elemental characterization, we can deduce that the Mn–Fe–N–C SAC prepared by an effective MnO_x engineering strategy is enriched in single iron sites and Fe–Mn/Fe–O–Mn bonds.

The ORR electrocatalytic performance was evaluated by using a rotating disk/ring-disk electrode (RDE/RRDE). At first, the optimization of pyrolysis temperature was achieved by performing 800–1000 °C parallel experiments (Fig. S10†). The Mn–Fe–N–C SAC upon 900 °C thermal treatment shows the best ORR performance in 0.1 M $HClO_4$. This is because carbon material pyrolysis at a relatively low temperature (800 °C) leads to lower conductivity while that at a relatively high temperature of 1000 °C results in the destruction of active sites.[45,46] Fig. 5a shows the RDE polarization curves of the Mn–Fe–N–C SAC and Fe–N–C SAC. The common Fe–N–C SAC has a good ORR performance with $E_{1/2}$ of 0.759 V. Compared to the Fe–N–C SAC, the Mn–Fe–N–C SAC prepared by the MnO_x engineering strategy exhibits a substantial improvement. The $E_{1/2}$ reaches as high as 0.799 V, representing one of the best ORR performances among the typically reported SACs (Table S2†). Nevertheless, the ORR activity of the Mn–Fe–N–C SAC is still poorer than that of Pt/C (Fig. S11†). The Tafel slope of the Mn–Fe–N–C SAC shown in Fig. 5b is slightly less steep than that of the Fe–N–C SAC, demonstrating that the MnO_x engineering process could significantly improve mass/charge transfer on the catalyst. Fig. 5c shows that the Mn–Fe–N–C SAC has much higher kinetic current densities (j_k) than those of the Fe–N–C SAC at all potentials. The turnover frequencies (TOFs) of the Mn–Fe–N–C SAC and Fe–N–C SAC and some representative reported single-atom catalysts were compared (Fig. 5d), and the Mn–Fe–N–C SAC showed an inimitable TOF as high as 1.54 e^- per site per s at 0.8 V, which is higher than those of the Fe–N–C SAC and some typical single-atom counterparts.[47–49] The enhanced ORR performance likely originates from a significant effect of the

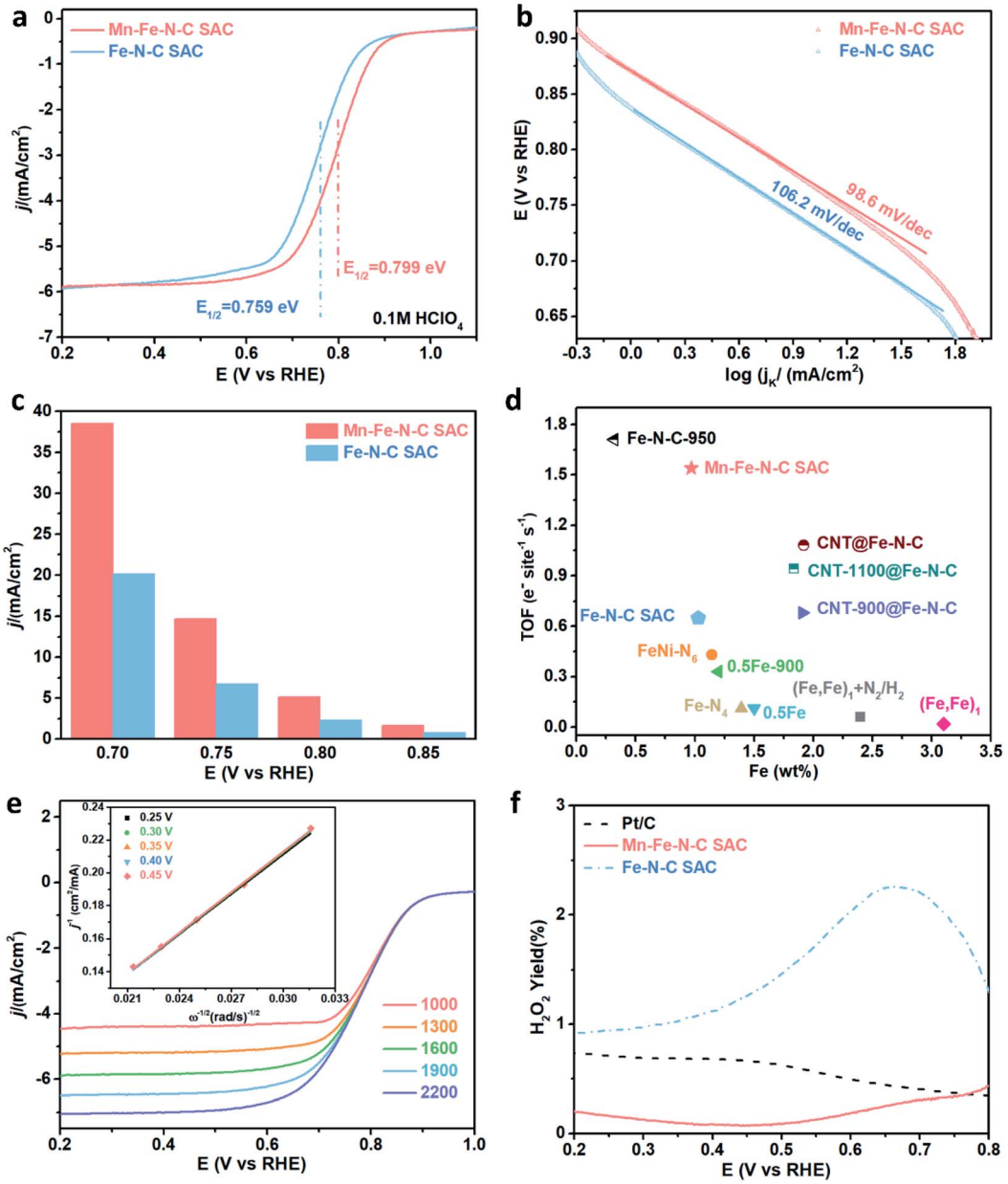

Fig. 5 (a) The RDE polarization curves for the Mn–Fe–N–C SAC and Fe–N–C SAC in 0.1 M $HClO_4$. (b) Tafel plots of the Fe–N–C SAC and Mn–Fe–N–C SAC. (c) Comparison of j_k of the different catalysts in O_2-saturated 0.1 M $HClO_4$. (d) Comparison of the Fe loading amount and turnover frequencies (TOFs) of the catalysts described in this work with single-atom catalysts reported previously at 0.8 V.[47–49] (e) RDE polarization curves at various rotating speeds for the Mn–Fe–N–C SAC in 0.1 M $HClO_4$. (The unit of rotating speed is rpm.) Inset: K–L plot of j^{-1} *versus* ω^{-1}. (f) H_2O_2 yields of the Mn–Fe–N–C SAC and Fe–N–C SAC.

MnO_x engineering method, modifying the coordination and electron structure of single-atom Fe sites.

RDE results of the Mn–Fe–N–C SAC were obtained at various rotation speeds from 1000 to 2200 rpm (Fig. 5e). The well-fitted parallel Koutecky–Levich (K–L) plots (inset of Fig. 5e) show good linearity (R^2 > 0.99) with a constant slope, indicating that the ORR processes follow first-order reaction kinetics mainly determined by the dissolved O_2 concentration. The average number of electrons transferred (n) by the Mn–Fe–N–C SAC from K–L plots is 3.98, which is larger than that of the Fe–N–C SAC (3.92) (Fig. S12†). This result reveals that the Mn–Fe–N–C SAC efficiently reduces O_2 *via* a direct four-electron pathway and has a much higher ORR efficiency than that of the conventional Fe–N–C SAC. Such a result is further demonstrated by RRDE measurements (Fig. S13†). Based on the Damjanovic model (Fig. S14†), the Mn–Fe–N–C SAC for the ORR prioritizes a four-electron-transfer pathway to form H_2O instead of H_2O_2 and therefore shows low H_2O_2 yield.[50] Besides, the produced H_2O_2 could be immediately decomposed by a disproportionation reaction on the Mn–Fe–N–C SAC, which also leads to low H_2O_2

yield. Calculated from the RRDE results, the H_2O_2 yield of the Mn–Fe–N–C SAC is ultralow, such as the maximum value is only 0.80% at a range of 0.2 V - 0.8 V, which is much lower than that of the Fe–N–C SAC (Fig. 5f). Such ultralow H_2O_2 yields suggest that the destruction of the catalyst structure and MEA from oxidation reactions such as the Fenton reaction could be greatly reduced, and therefore the Mn–Fe–N–C SAC is expected to exhibit good stability.

The stability of the SACs is one of the significant factors that will directly influence their further practical applicability. Here, the ORR stability was investigated by performing potential cycling tests and the results are shown in Fig. 6a. After 10000 continuous cycles, the $E_{1/2}$ of the Mn–Fe–N–C SAC shows a smaller negative shift (~6 mV) than that of the Fe–N–C SAC counterpart (~24 mV), which means that the MnO_x engineering can obviously enhance the ORR stability of the Fe–N_x sites. Besides, both SACs also show good resistance against methanol (Fig. S15†). Two series of colorimetric method-based tests were used to determine the mechanism of enhanced stability of the MnO_x engineered Fe–N–C SAC. At first, horseradish peroxidase (HRP) based colorimetric measurements (Fig. S16†) were used to detect the H_2O_2/ROS yield of the reacted electrolytes after potential cycling. Color changes are observed with the substrates 3,3′,5,5′-tetramethylbenzidine (TMB, blue) and *o*-phenylenediamine (OPD, yellow) (Fig. 6b and S17†), showing that H_2O_2 or ROS are produced by all of the catalysts.[51–53] The slightest color changes and the lowest UV-Vis absorption value were observed in the Mn–Fe–N–C SAC reacted electrolytes (Fig. 6b), which illustrates the lowest H_2O_2/ROS yield compared to those of the commercial Pt/C and traditional Fe–N–C SAC. Such a result demonstrates that MnO_x engineering of the Fe–N–C SAC can reduce the H_2O_2/ROS yield and therefore impart excellent ORR stability. Moreover, we suppose that the outstanding stability of the Mn–Fe–N–C SAC originates from the disproportionation reaction between MnO_x and H_2O_2 instead of some Fenton reaction, therefore suffering less from oxidative damage by ROS. To further reveal their nature, the Mn–Fe–N–C SAC and Fe–N–C SAC were added to two H_2O_2 solutions with the same concentration. As shown in Fig. 6c, numerous bubbles are observed in the H_2O_2 solution with the Mn–Fe–N–C SAC while this is not obvious with the Fe–N–C SAC, demonstrating that H_2O_2 is catalyzed into O_2 and H_2O by MnO_x *via* a disproportionation reaction. Furthermore, another set of colorimetric measurements was used to evaluate the ROS production level in these two H_2O_2 solutions containing the Mn–Fe–N–C SAC and Fe–N–C SAC (Fig. 6d). UV/Vis absorption curves show that the absorbance value of the Mn–Fe–N–C SAC is lower than that of the Fe–N–C SAC counterpart, thus unambiguously

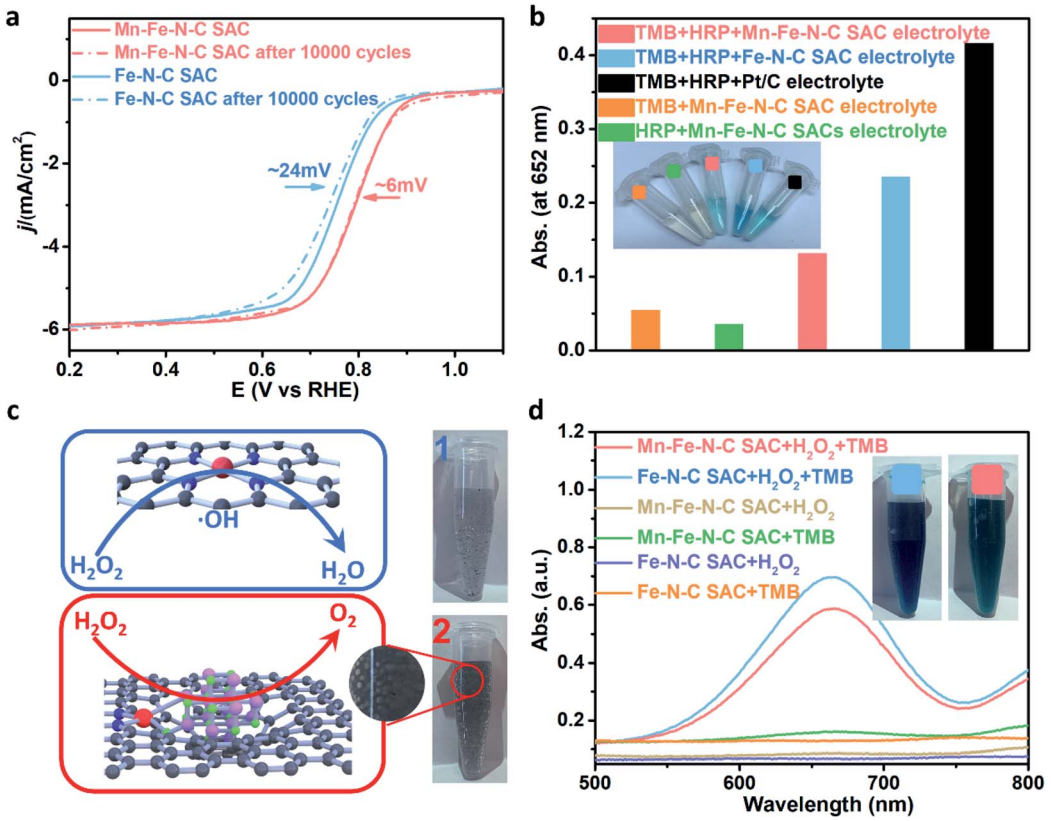

Fig. 6 (a) ORR polarization curves of the Mn–Fe–N–C SAC and Fe–N–C SAC before and after 10000 potential cycles. (b) Absorbance at 652 nm of different catalyst reacted ORR electrolytes by HRP detection with the substrate of TMB. Inset: photographs of the color changes (blue). (c) Schematic illustration of the Fenton reaction of the Fe–N–C SAC and disproportionation reaction of the Mn–Fe–N–C SAC. Inset: photographs of (1) Fe–N–C SAC + H_2O_2 and (2) Mn–Fe–N–C SAC + H_2O_2. (d) UV/Vis absorption curves of the Mn–Fe–N–C SAC and Fe–N–C SAC in solutions of TMB, H_2O_2, and TMB + H_2O_2, respectively. Inset: photographs of the color changes (blue).

demonstrating the suppression of ROS formation with the Mn–Fe–N–C SAC as the catalyst.[54] Based on these results, we can deduce that two main reasons led to the enhanced ORR stability of the MnO_x engineered Fe–N–C SAC. One is the lower H_2O_2 yield of the Mn–Fe–N–C SAC in the ORR process. The other is that the H–O bond of the H_2O_2 side-product is broken *via* a disproportionation reaction to form O_2 and H_2O, reducing the breaking of the O–O bond *via* the Fenton reaction to form strong oxidized ROS.

In conclusion, we have developed a MnO_x engineered Fe–N–C SAC (Mn–Fe–N–C SAC) to enhance the ORR stability of atomically dispersed iron–nitrogen–carbon catalysts under acidic conditions. MnO_x-coated iron-doped polypyrrole nanotubes were designed as the precursor. After pyrolysis, the obtained Mn–Fe–N–C SAC is enriched with single iron atomic sites accompanied by some MnO_x. Compared to the common Fe–N–C SAC, the Mn–Fe–N–C SAC shows a better ORR activity because the MnO_x modifies the coordination structure of single-atom Fe sites, possibly forming Fe–Mn or Fe–O–Mn bonds. Most importantly, the improved ORR stability by MnO_x engineering was investigated, and the mechanism was elucidated. Excellent long-term durability was obtained by the Mn–Fe–N–C SAC because of the lower H_2O_2 yield and decomposition of the yielded H_2O_2 by doped MnO_x, reducing the Fenton reaction's effects. Such properties endow the Mn–Fe–N–C SAC catalyst with huge potential for application in PEMFCs. This work provides a new strategy to solve the dilemma of the poor stability of Fe–N–C in PEMFCs.

Conflicts of interest

There are no conflicts to declare.

Acknowledgements

Lin Y. would like to acknowledge the support from a start-up fund of Washington State University. This research used resources of the Advanced Photon Source and the Center for Nanoscale Materials, Office of Science user facilities, supported by the U.S. Department of Energy, Office of Science, Office of Basic Energy Sciences, under Contract No. DE-AC02-06CH11357.

References

1 X. Xie, C. He, B. Li, Y. He, D. A. Cullen, E. C. Wegener, A. J. Kropf, U. Martinez, Y. Cheng and M. H. Engelhard, *Nat. Catal.*, 2020, 1–11.
2 Z. Shangguan, B. Li, P. Ming and C. Zhang, *J. Mater. Chem. A*, 2021, **9**, 15111–15139.
3 K. A. Stoerzinger, M. Risch, B. Han and Y. Shao-Horn, *ACS Catal.*, 2015, **5**, 6021–6031.
4 C. Chen, Y. Kang, Z. Huo, Z. Zhu, W. Huang, H. L. Xin, J. D. Snyder, D. Li, J. A. Herron and M. Mavrikakis, *Science*, 2014, **343**, 1339–1343.
5 J. Xue, Y. Li and J. Hu, *J. Mater. Chem. A*, 2020, **8**, 7145–7157.
6 C. Zhu, Q. Shi, B. Z. Xu, S. Fu, G. Wan, C. Yang, S. Yao, J. Song, H. Zhou, D. Du, S. P. Beckman, D. Su and Y. Lin, *Adv. Energy Mater.*, 2018, **8**, 1801956.
7 A. Morozan, B. Jousselme and S. Palacin, *Energy Environ. Sci.*, 2011, **4**, 1238–1254.
8 R. Jasinski, *Nature*, 1964, **201**, 1212–1213.
9 C. Zhu, S. Fu, Q. Shi, D. Du and Y. Lin, *Angew. Chem., Int. Ed.*, 2017, **56**, 13944–13960.
10 X.-F. Yang, A. Wang, B. Qiao, J. Li, J. Liu and T. Zhang, *Acc. Chem. Res.*, 2013, **46**, 1740–1748.
11 S. Ji, Y. Chen, X. Wang, Z. Zhang, D. Wang and Y. Li, *Chem. Rev.*, 2020, **120**, 11900–11955.
12 S. Ding, Z. Lyu, H. Zhong, D. Liu, E. Sarnello, L. Fang, M. Xu, M. H. Engelhard, H. Tian, T. Li, X. Pan, S. P. Beckman, S. Feng, D. Du, J.-C. Li, M. Shao and Y. Lin, *Small*, 2021, **17**, 2004454.
13 X. Wei, X. Luo, N. Wu, W. Gu, Y. Lin and C. Zhu, *Nano Energy*, 2021, **84**, 105817.
14 C. Zhu, Q. Shi, S. Feng, D. Du and Y. Lin, *ACS Energy Lett.*, 2018, **3**, 1713–1721.
15 X. Wan, X. Liu, Y. Li, R. Yu, L. Zheng, W. Yan, H. Wang, M. Xu and J. Shui, *Nat. Catal.*, 2019, **2**, 259–268.
16 X. Wang, H. Zhang, H. Lin, S. Gupta, C. Wang, Z. Tao, H. Fu, T. Wang, J. Zheng, G. Wu and X. Li, *Nano Energy*, 2016, **25**, 110–119.
17 J.-C. Li, F. Xiao, H. Zhong, T. Li, M. Xu, L. Ma, M. Cheng, D. Liu, S. Feng, Q. Shi, H.-M. Cheng, C. Liu, D. Du, S. P. Beckman, X. Pan, Y. Lin and M. Shao, *ACS Catal.*, 2019, **9**, 5929–5934.
18 Y. Jing and B. P. Chaplin, *Environ. Sci. Technol.*, 2017, **51**, 2355–2365.
19 Y. He, Q. Shi, W. Shan, X. Li, A. J. Kropf, E. C. Wegener, J. Wright, S. Karakalos, D. Su, D. A. Cullen, G. Wang, D. J. Myers and G. Wu, *Angew. Chem., Int. Ed.*, 2021, **60**, 9516–9526.
20 F. Cheng, Y. Su, J. Liang, Z. Tao and J. Chen, *Chem. Mater.*, 2010, **22**, 898–905.
21 G. Chen, J. Sunarso, Y. Zhu, J. Yu, Y. Zhong, W. Zhou and Z. Shao, *ChemElectroChem*, 2016, **3**, 1760–1767.
22 Q. Yu, J. Xu, C. Wu, J. Zhang and L. Guan, *ACS Appl. Mater. Interfaces*, 2016, **8**, 35264–35269.
23 C. Shang, M. Yang, Z. Wang, M. Li, M. Liu, J. Zhu, Y. Zhu, L. Zhou, H. Cheng, Y. Gu, Y. Tang, X. Zhao and Z. Lu, *Sci. China Mater.*, 2017, **60**, 937–946.
24 Y. Zhong, X. Liang, Z. He, W. Tan, J. Zhu, P. Yuan, R. Zhu and H. He, *Appl. Catal., B*, 2014, **150**, 612–618.
25 D. Deng, K. Novoselov, Q. Fu, N. Zheng, Z. Tian and X. Bao, *Nat. Nanotechnol.*, 2016, **11**, 218.
26 P. Hao, Z. Zhao, Y. Leng, J. Tian, Y. Sang, R. I. Boughton, C. Wong, H. Liu and B. Yang, *Nano Energy*, 2015, **15**, 9–23.
27 S. Yi, X. Qin, C. Liang, J. Li, R. Rajagopalan, Z. Zhang, J. Song, Y. Tang, F. Cheng, H. Wang and M. Shao, *Appl. Catal., B*, 2020, **264**, 118537.
28 P. Song, B. Liu, C. Liang, K. Ruan, H. Qiu, Z. Ma, Y. Guo and J. Gu, *Nano-Micro Lett.*, 2021, **13**, 91.
29 K. Ruan, Y. Guo, C. Lu, X. Shi, T. Ma, Y. Zhang, J. Kong and J. Gu, *Research*, 2021, **2021**, 8438614.

30 J. Wang and F. Ciucci, *Small*, 2017, **13**, 1604103.
31 K. S. Sing, *Pure Appl. Chem.*, 1985, **57**, 603–619.
32 L. I. Hill, A. Verbaere and D. Guyomard, *J. Power Sources*, 2003, **119**, 226–231.
33 J. Fan, Q. Ren, S. Mo, Y. Sun, M. Fu, J. Wu, L. Chen, P. Chen and D. Ye, *ChemCatChem*, 2020, **12**, 1046–1054.
34 T. H. Gu, D. A. Agyeman, S. J. Shin, X. Jin, J. M. Lee, H. Kim, Y. M. Kang and S. J. Hwang, *Angew. Chem., Int. Ed.*, 2018, **57**, 15984–15989.
35 W. Yang, Z. Su, Z. Xu, W. Yang, Y. Peng and J. Li, *Appl. Catal., B*, 2020, **260**, 118150.
36 H.-W. Liang, W. Wei, Z.-S. Wu, X. Feng and K. Müllen, *J. Am. Chem. Soc.*, 2013, **135**, 16002–16005.
37 Y. Zhu, B. Zhang, X. Liu, D. W. Wang and D. S. Su, *Angew. Chem.*, 2014, **126**, 10849–10853.
38 Z. Lyu, S. Ding, N. Zhang, Y. Zhou, N. Cheng, M. Wang, M. Xu, Z. Feng, X. Niu, Y. Cheng, C. Zhang, D. Du and Y. Lin, *Research*, 2020, **2020**, 4724505.
39 J.-C. Li, X. Qin, F. Xiao, C. Liang, M. Xu, Y. Meng, E. Sarnello, L. Fang, T. Li, S. Ding, Z. Lyu, S. Zhu, X. Pan, P.-X. Hou, C. Liu, Y. Lin and M. Shao, *Nano Lett.*, 2021, **21**, 4508–4515.
40 S. Ding, Z. Lyu, L. Fang, T. Li, W. Zhu, S. Li, X. Li, J.-C. Li, D. Du and Y. Lin, *Small*, 2021, **17**, 2100664.
41 D. Liu, J.-C. Li, S. Ding, Z. Lyu, S. Feng, H. Tian, C. Huyan, M. Xu, T. Li, D. Du, P. Liu, M. Shao and Y. Lin, *Small Methods*, 2020, **4**, 1900827.
42 L. Bainsla, A. Yadav, Y. Venkateswara, S. Jha, D. Bhattacharyya and K. Suresh, *J. Alloys Compd.*, 2015, **651**, 509–513.
43 Z. Chen, X. Liao, C. Sun, K. Zhao, D. Ye, J. Li, G. Wu, J. Fang, H. Zhao and J. Zhang, *Appl. Catal., B*, 2021, **288**, 120021.
44 M. Zhang, Y.-G. Wang, W. Chen, J. Dong, L. Zheng, J. Luo, J. Wan, S. Tian, W.-C. Cheong and D. Wang, *J. Am. Chem. Soc.*, 2017, **139**, 10976–10979.
45 R. Du, N. Zhang, J. Zhu, Y. Wang, C. Xu, Y. Hu, N. Mao, H. Xu, W. Duan and L. Zhuang, *Small*, 2015, **11**, 3903–3908.
46 P. Yin, T. Yao, Y. Wu, L. Zheng, Y. Lin, W. Liu, H. Ju, J. Zhu, X. Hong and Z. Deng, *Angew. Chem.*, 2016, **128**, 10958–10963.
47 U. I. Kramm, I. Herrmann-Geppert, J. Behrends, K. Lips, S. Fiechter and P. Bogdanoff, *J. Am. Chem. Soc.*, 2016, **138**, 635–640.
48 J.-C. Li, D.-M. Tang, P.-X. Hou, G.-X. Li, M. Cheng, C. Liu and H.-M. Cheng, *MRS Commun.*, 2018, **8**, 1158–1166.
49 Y. Zhou, W. Yang, W. Utetiwabo, Y.-m. Lian, X. Yin, L. Zhou, P. Yu, R. Chen and S. Sun, *J. Phys. Chem. Lett.*, 2020, **11**, 1404–1410.
50 F. Wu, C. Pan, C.-T. He, Y. Han, W. Ma, H. Wei, W. Ji, W. Chen, J. Mao and P. Yu, *J. Am. Chem. Soc.*, 2020, **142**, 16861–16867.
51 S. Ding, N. Zhang, Z. Lyu, W. Zhu, Y.-C. Chang, X. Hu, D. Du and Y. Lin, *Mater. Today*, 2021, **43**, 166–184.
52 Z. Lyu, S. Ding, M. Wang, X. Pan, Z. Feng, H. Tian, C. Zhu, D. Du and Y. Lin, *Nano-Micro Lett.*, 2021, **13**, 146.
53 L. Jiao, W. Xu, Y. Wu, H. Yan, W. Gu, D. Du, Y. Lin and C. Zhu, *Chem. Soc. Rev.*, 2021, **50**, 750–765.
54 E. Luo, H. Zhang, X. Wang, L. Gao, L. Gong, T. Zhao, Z. Jin, J. Ge, Z. Jiang, C. Liu and W. Xing, *Angew. Chem., Int. Ed.*, 2019, **58**, 12469–12475.